A new method to measure galaxy bias by combining the density and weak lensing fields

Arnau Pujol[⋆][1], Chihway Chang[2], Enrique Gaztañaga[1], Adam Amara[2],
Alexandre Refregier[2], David J. Bacon[3], Jorge Carretero[1,4], Francisco J. Castander[1],
Martin Crocce[1], Pablo Fosalba[1], Marc Manera[5], Vinu Vikram[6,7]

[1] *Institut de Ciències de l'Espai (ICE, IEEC/CSIC), E-08193 Bellaterra (Barcelona), Spain*
[2] *Department of Physics, ETH Zurich, Wolfgang-Pauli-Strasse 16, CH-8093 Zurich, Switzerland*
[3] *Institute of Cosmology and Gravitation, University of Portsmouth, Dennis Sciama Building, Portsmouth, PO1 3FX, U.K.*
[4] *Institut de Física d'Altes Energies, Universitat Autònoma de Barcelona, E-08193 Bellaterra, Barcelona, Spain*
[5] *University College London, Gower Street, London, WC1E 6BT, U.K*
[6] *Argonne National Laboratory, 9700 South Cass Avenue, Lemont, IL 60439, USA*
[7] *Department of Physics and Astronomy, University of Pennsylvania, Philadelphia, PA 19104, USA*

ABSTRACT

We present a new method to measure the redshift-dependent galaxy bias by combining information from the galaxy density field and the weak lensing field. This method is based on Amara et al. (2012), where they use the galaxy density field to construct a bias-weighted convergence field κ_g. The main difference between Amara et al. (2012) and our new implementation is that here we present another way to measure galaxy bias using tomography instead of bias parameterizations. The correlation between κ_g and the true lensing field κ allows us to measure galaxy bias using different zero-lag correlations, such as $\langle \kappa_g \kappa \rangle / \langle \kappa \kappa \rangle$ or $\langle \kappa_g \kappa_g \rangle / \langle \kappa_g \kappa \rangle$. This paper is the first that studies and systematically tests the robustness of this method in simulations. We use the MICE simulation suite, which includes a set of self-consistent N-body simulations, lensing maps, and mock galaxy catalogues. We study the accuracy and systematic uncertainties associated with the implementation of the method, and the regime where it is consistent with the linear galaxy bias defined by projected 2-point correlation functions (2PCF). We find that our method is consistent with linear bias at the percent level for scales larger than 30 arcmin, while nonlinearities appear at smaller scales. We also find that projection along the redshift direction can cause up to a 5% deviation between the different galaxy bias estimators. This measurement is a good complement to other measurements of bias, since it does not depend strongly on σ_8 as the 2PCF measurements. We apply this method to the Dark Energy Survey Science Verification data in a follow-up paper.

Key words: gravitational lensing: weak; surveys; cosmology: large-scale structure

1 INTRODUCTION

The formation and evolution of the large scale structures in the Universe is an important tool for cosmology studies. But since most of the mass in the Universe is in the form of dark matter, which cannot be directly observed, we need

to understand the connection between the observable universe (galaxies and stars) and dark matter. In the ΛCDM paradigm, structures form in the initial density peaks causing dark matter to gravitationally collapse and form virialized objects. Galaxies are expected to follow these gravitational potentials (e.g. White & Rees 1978), and because of this they are tracers of the dark matter density peaks. The relation between the galaxy and mass distributions can

⋆ E-mail: pujol@ice.cat

be described theoretically with the galaxy bias prescription (Kaiser 1984; Fry & Gaztanaga 1993; Bernardeau 1996; Mo & White 1996; Sheth & Tormen 1999; Manera, Sheth & Scoccimarro 2010; Manera & Gaztañaga 2011). Galaxy bias allows us to connect the distribution of galaxies with that of dark matter, and a good knowledge of galaxy bias would be very important to improve the precision of our cosmological measurements (Eriksen & Gaztanaga 2015).

Many papers have studied halo and galaxy bias in simulations (Cole & Kaiser 1989; Kravtsov & Klypin 1999; Seljak & Warren 2004; Angulo, Baugh & Lacey 2008; Faltenbacher & White 2010; Tinker et al. 2010; Manera & Gaztañaga 2011; Paranjape et al. 2013; Pujol & Gaztañaga 2014; Zentner, Hearin & van den Bosch 2014; Carretero et al. 2015; Pujol et al. 2015), and the different ways to measure bias (Kravtsov & Klypin 1999; Bernardeau et al. 2002; Manera & Gaztañaga 2011; Roth & Porciani 2011; Pollack, Smith & Porciani 2014; Hoffmann et al. 2015; Bel, Hoffmann & Gaztañaga 2015). There are also several measurements of bias in observations where usually the dark matter clustering is assumed from a model or from simulations (Zehavi et al. 2011; Coupon et al. 2012; Cacciato et al. 2012; Jullo et al. 2012; Marín et al. 2013; Durkalec et al. 2014; Di Porto et al. 2014). In most of these studies, however, the results depend strongly on assumptions of the cosmological parameters.

Gravitational lensing is the effect of light deflection due to the perturbations in the gravitational potential from mass distribution. It is a powerful tool to measure the mass distribution in the Universe, since the gravitational potential is affected by both baryonic and dark matter. Weak lensing refers to the statistical study of small distortions (around 1%) in the shapes of a large number of galaxies due to this effect. Several ongoing and future galaxy surveys aim to obtain large weak lensing data sets that will allow us to better constrain cosmology, including the Hyper Suprime-Cam (HSC; Miyazaki et al. 2006), the Dark Energy Survey (DES; The Dark Energy Survey Collaboration 2005; Flaugher 2005), the Kilo Degree Survey (KIDS; de Jong et al. 2013), the Panoramic Survey Telescope and Rapid Response System (PanSTARRS; Kaiser et al. 2010), the Large Synoptic Survey Telescope (LSST; LSST Science Collaboration et al. 2009), Euclid (Laureijs et al. 2011), and Wide-Field Infrared Survey Telescope (WFIRST; Green et al. 2012). From the shape of the galaxies one can statistically infer the lensing fields, which contain information of the projected matter distribution and can be used to generate 2D and 3D mass maps (Massey et al. 2007; Van Waerbeke et al. 2013; Vikram et al. 2015).

The combination of weak lensing and galaxy density information gives us a powerful handle for measuring galaxy bias. Amara et al. (2012) used the COSMOS field to measure galaxy bias by reconstructing a bias-weighted shear map from the galaxy density field. The galaxy bias is estimated from the zero-lag cross correlation between this bias-weighted shear map from the galaxy density field and the shear measured from galaxy shapes. Different parameterizations of bias are used to measure constant, non-linear and redshift-dependent bias. In this paper we explore and extend the method from Amara et al. (2012). We analyze whether the galaxy bias measured with our method is consistent with the linear bias obtained from the projected 2-point correlation functions (2PCF). We find that our method can be affected by different parameters in the implementation such as redshift binning, the redshift range used, angular scales, survey area and shot noise. Finally, we show how to measure the redshift-dependent galaxy bias by using tomographic redshift binning. Although this method is very similar to the one presented in Amara et al. (2012), there are few notable differences. First of all, in Amara et al. (2012) they explore different smoothing schemes for the density field, while we explore pixelizing the maps and applying a Top Hat filter. In Amara et al. (2012) the lensing shear is estimated for each galaxy, and the bias is measured from the predicted and measured shear of the galaxies, while we measure galaxy bias from the generated lensing maps. Finally, Amara et al. (2012) fit different parametric biases using a wide range of redshift for the galaxy density field, while here we implement a tomographic measurement, where we measure bias in redshift bins by using the density field of galaxies in each particular bin. We will apply this method to the DES Science Verification (SV) data in a second paper (Chang et al. in prep, hereafter Paper II).

The paper is organized as follows. In §2 we give an overview of the theory for our analysis. In §3 we present the method used to measure bias from the galaxy density and weak lensing fields and the numerical effects associated with the implementation of the method. In §4 we present the results of the different tests and the final measurement of redshift-dependent galaxy bias. We finally close in §5 with discussion and conclusions.

2 THEORY

2.1 Galaxy Bias

The distribution of galaxies traces that of dark matter, and one of the common descriptions for this relation is galaxy bias, which relates the distribution of galaxies with that of dark matter. There are several ways to quantify galaxy bias (Bernardeau et al. 2002; Manera & Gaztañaga 2011; Roth & Porciani 2011; Hoffmann et al. 2015; Bel, Hoffmann & Gaztañaga 2015), and one of the most common ones is from the ratio of the 2PCFs of galaxies and dark matter:

$$\xi_g(r) = b^2(r)\xi(r), \tag{1}$$

where $b(r)$ is the galaxy bias, and $\xi_g(r)$ and $\xi(r)$ are the scale-dependent galaxy and matter 2PCFs respectively, which are defined as:

$$\xi_g(r_{12}) = \langle \delta_g(\boldsymbol{r_1})\delta_g(\boldsymbol{r_2}) \rangle, \ \xi(r_{12}) = \langle \delta(\boldsymbol{r_1})\delta(\boldsymbol{r_2}) \rangle. \tag{2}$$

where $\delta_g = (\rho_g - \bar{\rho}_g)/\bar{\rho}_g$ is the density fluctuation of galaxies (ρ_g is the galaxy number density), and $\delta = (\rho - \bar{\rho})/\bar{\rho}$ is the density fluctuation of dark matter (ρ is the dark matter density). As can be seen from this equation, galaxy bias generally depends on the scale r_{12} (defined as the distance between $\boldsymbol{r_1}$ and $\boldsymbol{r_2}$). However, it has been shown that at

sufficiently large scales in the linear bias regime, bias is constant (e.g. Manera & Gaztañaga 2011).

Bias can also be defined from the projected 2PCFs:

$$\omega_g(\Theta) = b^2(\Theta)\omega(\Theta), \tag{3}$$

where $\omega_g(\Theta)$ and $\omega(\Theta)$ refer to the projected 2PCF of galaxies and dark matter respectively. This definition of bias will be used in the analysis of this paper. In this case, the bias dependence is on angle Θ instead of distance r.

In the local bias model approach (Fry & Gaztanaga 1993), the density field of galaxies is described as a function of its local dark matter density, so that $\delta_g = F[\delta]$. We can express this relation as a Taylor series:

$$\delta_g = b_0 + b_1\delta + \frac{b_2}{2}\delta^2 + ... = \sum_{i=0}^{\infty} b_i(z)\delta^i, \tag{4}$$

where b_i are the coefficients of the Taylor expansion. In the linear regime, $\delta \ll 1$, and as $b_0 = 0$ because $\langle\delta_g\rangle = \langle\delta\rangle = 0$, then the equation becomes:

$$\delta_g = b_1\delta \tag{5}$$

According to Manera & Gaztañaga (2011), at large scales this definition of bias is consistent with the bias obtained from the 2PCFs: for $r_{12} \gtrsim 40\,h^{-1}\,\mathrm{Mpc}$, b from equation (1) is indeed constant and equivalent to b_1 from equation (5). This b_1 can then be measured from the different zero-lag correlations between δ_g and δ:

$$b_1 = \frac{\langle\delta_g\delta\rangle}{\langle\delta\delta\rangle} \tag{6}$$

$$b_1 = \frac{\langle\delta_g\delta_g\rangle}{\langle\delta_g\delta\rangle} \tag{7}$$

$$b_1 = \sqrt{\frac{\langle\delta_g\delta_g\rangle}{\langle\delta\delta\rangle}} \tag{8}$$

Although these relations appear to measure the same parameter b_1, the results can be affected by the stochasticity in the relation between δ_g and δ, that can come from different effects, such as the intrinsic stochasticity of bias and the projection effects.

Galaxy bias from equations (6-8) depend on the smoothing angular scale θ used to measure δ and δ_g. For small angle θ nonlinearities in the relation between δ and δ_g appear, and b_1 is no longer consistent with equation (3). The relation between both scales of bias Θ and θ is complex, since the smoothing of δ and δ_g involves the correlations of all the scales below θ. However, in the linear and local regime bias is constant in both θ and Θ and then all the estimators can be compared.

2.2 Weak Lensing

Weak gravitational lensing (see e.g. Bartelmann & Schneider 2001; Refregier 2003) measures the small changes of galaxy shapes and brightnesses due to the foreground mass distribution in the line-of-sight of the (source) galaxies. By studying

this effect statistically, assuming that (lensed) galaxies are randomly oriented in the absence of lensing, one can infer the mass distribution in the foreground of these source galaxies. As the light distortion is affected by gravity, weak lensing allows us to measure the total mass distribution, including baryonic and dark matter.

The gravitational potential Φ of a given density distribution δ can be defined as:

$$\nabla^2\Phi = \frac{3H_0^2\Omega_m}{2a}\delta, \tag{9}$$

where H_0 and Ω_m are the Hubble parameter and the matter density today, and a is the scale factor assuming a spatially flat Universe. Assuming General Relativity and no anisotropic stress, the lensing potential for a given source at position $(\boldsymbol{\theta}, \chi_s)$ is given by the weighted line-of-sight projection of Φ:

$$\psi(\boldsymbol{\theta}, \chi_s) = 2\int_0^{\chi_s} d\chi \frac{\chi(\chi_s - \chi)}{\chi_s}\Phi(\boldsymbol{\theta}, \chi), \tag{10}$$

where $\boldsymbol{\theta}$ is the angular position on the sky, χ refers to the comoving radius and χ_s is the comoving distance to the sources. The distortion of the source galaxy images can be described by the convergence κ and shear $\boldsymbol{\gamma}$ fields that are defined as:

$$\kappa = \frac{1}{2}\nabla^2\psi, \tag{11}$$

$$\boldsymbol{\gamma} = \gamma_1 + i\gamma_2 = \frac{1}{2}(\psi_{,11} - \psi_{,22}) + i\psi_{,12}, \tag{12}$$

where $\psi_{,ij} = \partial_i\partial_j\psi$. Focusing on the convergence field, combining equations (9), (10) and (11) we obtain:

$$\kappa(\boldsymbol{\theta}, \chi_s) = \frac{3H_0^2\Omega_m}{2c^2}\int_0^{\chi_s} d\chi \frac{\chi(\chi_s - \chi)}{\chi_s}\frac{\delta(\boldsymbol{\theta}, \chi)}{a(\chi)} \equiv K[\delta] \tag{13}$$

For simplicity, we define $q(\chi)$ as the lensing kernel of the integral of δ at χ:

$$q(\chi, \chi_s) = \frac{3H_0^2\Omega_m}{2c^2}\frac{\chi(\chi_s - \chi)}{\chi_s a(\chi)} \tag{14}$$

so that

$$\kappa(\boldsymbol{\theta}, \chi) = \int_0^{\chi_s} q(\chi, \chi_s)\delta(\boldsymbol{\theta}, \chi)d\chi. \tag{15}$$

Note that κ corresponds to a weighted integral of the matter density fluctuations in the line-of-sight of the source galaxies.

3 METHOD

3.1 Simulation

For the analysis we use the MICE Grand Challenge simulation (Fosalba et al. 2015a,b; Crocce et al. 2015b), an N-body simulation of a ΛCDM cosmology with the following cosmological parameters: $\Omega_m = 0.25$, $\sigma_8 = 0.8$, $n_s = 0.95$, $\Omega_b = 0.044$, $\Omega_\Lambda = 0.75$, $h = 0.7$. It has a volume of $(3.072\,h^{-1}\,\mathrm{Gpc})^3$ with 4096^3 particles of mass $2.927 \times 10^{10}\,h^{-1}\,\mathrm{M_\odot}$. The galaxy catalogue has been run according to a Halo Occupation Distribution (HOD) and a

SubHalo Abundance Matching (SHAM) prescriptions (Carretero et al. 2015). The parameters of the model have been fitted to reproduce clustering as a function of luminosity and colour from the Sloan Digital Sky Survey (Zehavi et al. 2011), as well as the luminosity function (Blanton et al. 2003, 2005a) and colour-magnitude diagrams (Blanton et al. 2005b). We use the MICECATv2 catalogue, an extension of the publicly available MICECATv1 catalogue[1]. The galaxy catalogue is complete for $i < 24$ from $z = 0.07$ to $z = 1.4$. The catalogue also contains the lensing quantities (γ_1, γ_2 and κ) at the position of each galaxy, calculated from the dark matter field with a resolution of Nside=8192 in healpix (corresponding to a pixel size of ~ 0.43 arcmin), so the lensing quantities of the galaxies do not have shape noise.

3.2   Bias estimation

In this section, we introduce the method used to estimate galaxy bias from the lensing and density maps of galaxies in the MICE simulation. It consists on the construction of a template κ_g for the lensing map κ from the density distribution of the foreground galaxies assuming equation (5). Substituting δ with δ_g in equation (13) gives:

$$\kappa_g(\boldsymbol{\theta}) \simeq K[\delta_g] = \int_0^{\chi_s} q(\chi, \chi_s)\delta_g(\boldsymbol{\theta}, \chi)d\chi \qquad (16)$$

When computing κ_g numerically, the integral becomes a sum over all lenses in the foreground of the sources:

$$\kappa_g(\boldsymbol{\theta}) = \sum_{all\ lens\ bins} \bar{q}'\delta_g'(\boldsymbol{\theta})\Delta\chi', \qquad (17)$$

where we have split the foreground galaxies into redshift bins. $\Delta\chi'$ refers to each redshift bin width in comoving coordinates, $\bar{q}'$ is the mean lensing weight that corresponds to each redshift bin and $\delta_g'(\boldsymbol{\theta})$ is the galaxy density fluctuation in each redshift bin at position $\boldsymbol{\theta}$, where $\boldsymbol{\theta}$ now represents a pixel in the sky plane. $\delta_g'(\boldsymbol{\theta})$ is calculated through $\delta_g'(\boldsymbol{\theta}) = (\rho_g'(\boldsymbol{\theta}) - \bar{\rho}_g')/\bar{\rho}_g'$, where $\rho_g'(\boldsymbol{\theta})$ is the density of galaxies projected in the line-of-sight in each redshift bin and position (pixel) $\boldsymbol{\theta}$. Notice that $\delta_g'(\boldsymbol{\theta})$ is calculated taking into account all the galaxies inside the volume of the cell corresponding to each pixel and redshift bin. This means that $\delta_g'(\boldsymbol{\theta})$ is constant inside the bin, and it corresponds to a projection of the galaxy density weighted by the volume of the corresponding cell.

In Figure 1 we show a schematic picture of the effects of equation (17). Dahsed black line shows $q(z, z_s)$, while red solid line shows $\bar{q}'$ in redshift bins of $\Delta z = 0.2$. We used $z_s = 1.3$ for this figure. The blue shaded region represents $\delta_g(z)$ in a random (just for the example) pixel in the sky using narrow redshift bins ($\Delta z = 0.05$). The blue solid line represents δ_g' for the redshift bins of $\Delta z = 0.2$. Equation (17) then is equivalent to the integral of the product of the blue and red solid lines.

Equation (17) is an approximation of (16), that assumes that the small fluctuations in redshift of δ_g inside the bins do not affect the results. It also assumes that the mean of
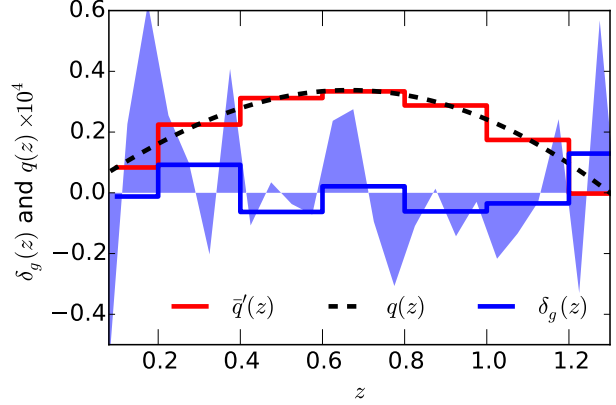
Figure 1. Schematic comparison of equations (16,17). Dahsed black line shows $q(z, z_s)$, while red solid line shows $\bar{q}'$ from equation (17) in redshift bins of $\Delta z = 0.2$. The blue shaded region represents $\delta_g(z)$ using narrow redshift bins ($\Delta z = 0.05$). The blue solid line represents δ_g' for the redshift bins of $\Delta z = 0.2$.

$q(\chi)\delta_g(\chi)$ inside the bins is equivalent to the product of the means $\bar{q}'\delta_g'(\boldsymbol{\theta})$. These approximations are correct at large scales and when $q'(\chi)$ and $\delta_g(\chi)$ are not correlated.

We focus on the simplest case, where the galaxy bias is linear, local and redshift-independent. In this case, we can estimate b from the following zero-lag correlations of κ and κ_g:

$$b = \frac{\langle\kappa_g\kappa\rangle}{\langle\kappa\kappa\rangle - \langle\kappa^N\kappa^N\rangle} \qquad (18)$$

$$b = \frac{\langle\kappa_g\kappa_g\rangle - \langle\kappa_g^N\kappa_g^N\rangle}{\langle\kappa_g\kappa\rangle}, \qquad (19)$$

where κ^N and κ_g^N are the sampling and shot-noise correction factors obtained by randomizing the galaxy positions and re-calculating κ and κ_g. κ is obtained from the mean κ of the galaxies in each pixel. This is affected by the number of source galaxies in the pixel, causing a noise in $\langle\kappa\kappa\rangle$ that depends on the angular resolution used, reaching a 10% error for a pixel size of 5 arcmin. This noise is cancelled by subtracting $\langle\kappa^N\kappa^N\rangle$. On the other hand, $\langle\kappa_g\kappa_g\rangle$ is affected by shot noise, causing an error that increases with the angular resolution up to a 20% for a pixel size of 5 arcmin. This noise is cancelled by subtracting $\langle\kappa_g^N\kappa_g^N\rangle$. This correction assumes a Poisson distribution. To test how well this correction works for this method, we calculated $\langle\kappa_g\kappa_g\rangle - \langle\kappa_g^N\kappa_g^N\rangle$ using the dark matter particles instead of galaxies, and we compared the results with the true $\langle\kappa\kappa\rangle$ maps from the simulation. We did this with different dilutions (from 1/70 to 1/700) of the dark matter particles, and recover $\langle\kappa\kappa\rangle$ better than 1% independently on the dilution, indicating that the shot-noise subtraction is appropriate.

These are the estimators of bias used in this paper. Since the galaxies used from the MICE simulation do not have shape noise, the estimators in this analysis are not affected by shape noise. This is not the case in observations, where

shape noise is the most important source of noise of this method and needs to be corrected.

To measure the errors on b, we use the Jack-Knife (JK) method. We divide the area into 16 subsamples. We evaluate b 16 times excluding each time a different subsample. The error of b is estimated from the standard deviation of these 16 measurements as:

$$\sigma(b) \simeq \sqrt{\frac{N_{JK} - 1}{N_{JK}} \sum_{i=1}^{N_{JK}} (b_i - \bar{b})^2}, \tag{20}$$

where N_{JK} refers to the number of Jack-Knife subsamples used and b_i is the bias measured by excluding the *ith* subsample. We checked that the error does not change if we use a different number of subsamples (between 9 and 100) instead of 16.

Note that we can also measure bias from the following cross correlations, which was originally used in Amara et al. (2012):

$$b = \frac{\langle \gamma_{i,g} \gamma_i \rangle}{\langle \gamma_i \gamma_i \rangle - \langle \gamma_i^N \gamma_i^N \rangle} \tag{21}$$

$$b = \frac{\langle \gamma_{i,g} \gamma_{i,g} \rangle - \langle \gamma_{i,g}^N \gamma_{i,g}^N \rangle}{\langle \gamma_{i,g}^N \gamma_i^N \rangle}, i = 1, 2 \tag{22}$$

As this is not the focus of the paper, and we can obtain κ from the simulation, we measure b from equations (18,19) in this study. However, in observations we measure the shape of the galaxies, that is directly related to γ_i. Because of this, applying this method to data requires a conversion from κ_g to $\gamma_{i,g}$ or from γ_i to κ. We address this issue in Paper II, where we use conversions based on Kaiser & Squires (1993) to apply this method to DES SV data. Another aspect to take into account for data analysis is that since shape noise is the main source of noise in the measurement, we like to avoid the terms that involve variance of lensing quantities $\langle \kappa \kappa \rangle$ and $\langle \gamma_i \gamma_i \rangle$, since these terms are the most affected by shape noise.

3.3 Implementation

In Figure 2, we illustrate our procedure. We used a ~ 900 square degree area from the MICE simulation corresponding to $0° < RA < 30°$ and $0° < DEC < 30°$. The top panel shows the convergence map κ, located at $z \simeq 1$. The middle panel shows the constructed convergence template, κ_g, derived via equation (17). Both maps have been smoothed using a circular top hat filter of 50 arcmin radius. We can see that κ_g is a biased version of κ at large scales. In the bottom panel we show the scatter plot of κ versus κ_g, using pixels of 7 arcmin of side in each map. The bias b shown in the plot is estimated via equation (18), and the error corresponds to the Jack-Knife errors from equation (20). In red, we show a line crossing the origin and with the slope corresponding to this estimated bias. We have checked that the b value derived from the zero-lag statistics is in agreement with a linear fit to the scatter plot at the 0.1% level. This is another indication that we are in the linear regime, where we can assume equation (5).
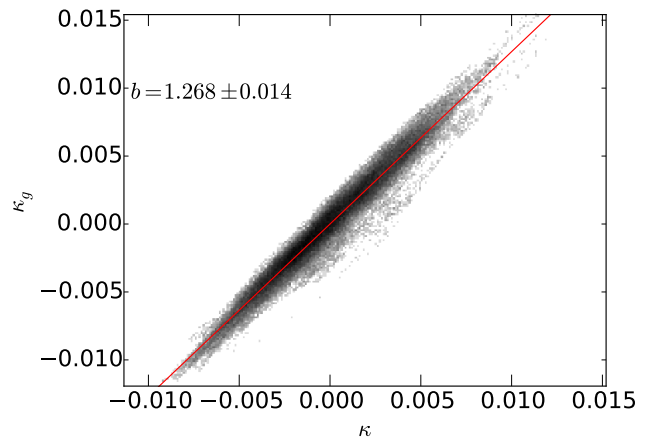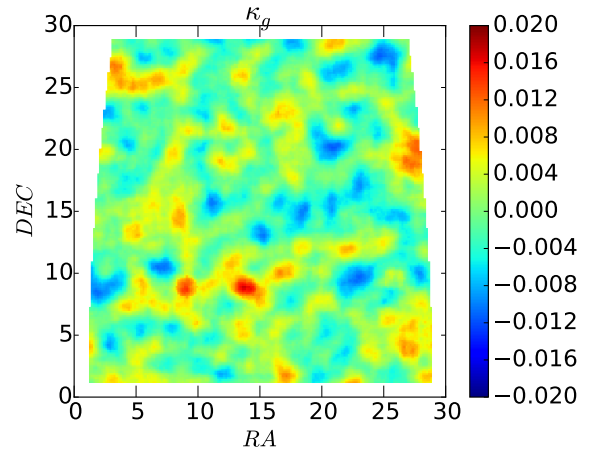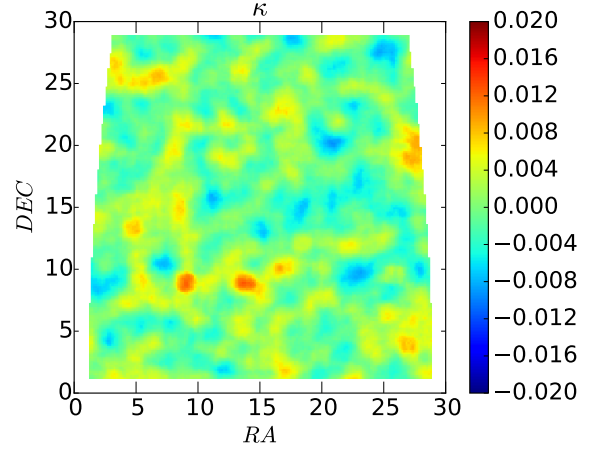

Figure 2. Comparison of κ vs κ_g. Top panel shows the κ field from the source galaxies within $0.9 < z < 1.1$ and using a Top Hat filter of 50 arcmin of radius. Middle panel shows κ_g obtained from equation (17), using the same smoothing scheme. Bottom panel shows the comparison between κ_g and κ for the pixels of the maps, with the specified bias and error obtained. The red line corresponds to a line crossing the origin and its slope corresponds to b. It is consistent with the linear fit of the distribution of the points.

We note that the expression for the bias from equations (18,19) assumes equation (5). However, κ is a projection of δ in the line-of-sight weighted by the lensing kernel, as well as κ_g. Thus, the relation between κ and κ_g is a constant that comes from the redshift dependence of bias weighted by the redshift dependence of the lensing kernel. Hence, the bias obtained in this example is a weighted mean of galaxy bias as a function of redshift. But we can take this dependence into account to measure bias at different redshifts using tomography as we explain in §3.5 below.

3.4   Numerical effects and parameters

There are different parameters that can affect our implementation presented in §3.2. We have studied in which regime our method is valid, or consistent with the linear bias from equation (3), and what are the dependences when it is not valid. With this, we can either calibrate our results or restrict to the regimes where our bias measurement is carried out. Here we describe the main numerical effects and our choice of parameters for our implementation.

Catalogue selection

We used an area of $0^o < RA, DEC < 30^o$. This is the same area we used for the fiducial bias measurements from equation (3), so that our comparison of both bias is not affected by differences in area or sample variance. This area is similar to DES Y1 data, so this study can be seen as an estimation of the theoretical limitations of this method on DES Y1.

We apply a magnitude cut for the foreground galaxies of $i < 22.5$, to be able to compare it with measurements in the DES SV data (Crocce et al. 2015a, Paper II). However, other selections can be done for this method, such us selecting galaxies by colour or luminosity, in order to measure colour and luminosity dependent bias, that would give information about galaxy formation and evolution.

Redshift bin width

We use redshift bins of $\Delta z = 0.2$ for the foreground galaxies. In this analysis we use the true redshift from the simulation, but in data this method would be also affected by photo-z errors.

For the choice of Δz we need to take into account two effects. On one side, the use of wide redshift bins would mean losing information from the small scale fluctuations of δ_g in the line-of-sight, since we project the galaxies in the same bin to measure δ_g. We have seen that this produces a deviation in the value of galaxy bias that is larger than 5% for $\Delta z > 0.2$, and it can be larger than 10% for $\Delta z > 0.3$. We explore this in Figure (5) and in §4.1. We take this effect into account when we estimate bias in tomographic bins at the end of the paper. When we have photo-z errors, the redshift binning effect is not as important as for the ideal case. If the photo-z errors dominate, the dilution of the small scale fluctuations come from the photo-z errors, and the redshift binning does not affect much. We address the effects of photo-z errors in Paper II.

On the other hand, the use of narrow redshift bins requires a smoothing of the estimation of $\bar{\rho}_g(z)$. If we calculate $\bar{\rho}_g$ for each redshift bin alone, for narrow bins $\bar{\rho}_g(z)$ is affected by the structure fluctuation in each particular redshift bin, and this causes a smoothing in the final estimation of δ_g. Some smoothing of $\bar{\rho}_g$ in redshift is needed to avoid this effect when using narrow bins. This is relevant for $\Delta z < 0.03$.

Angular scale

To generate the maps we pixelize the sky using a sinusoidal projection (which consists on redefining RA as $(RA - 15)\cos(DEC)$ in order to obtain a symmetric map with pixels of equal area) with an angular resolution of 50 arcmin, so that the area of the pixels is $(50 \text{ arcmin})^2$. Then galaxies are projected in different redshift bins according to their true redshift.

The bias estimated from this method is not necessarily consistent with the bias from equation (3) at small scales. These two methods are only expected to agree at large scales, in the linear bias regime. Moreover, this method requires a projection in the line-of-sight, so that different scales (weighted differently according to the lensing kernel) are mixed for the same angular scale. However, we have seen that bias is constant for angular scales larger than $\Theta \gtrsim 30$ arcmin, meaning that linear scales are dominant in this regime. In Figure 3 we show the agreement of galaxy bias between equations (3) and (6-8) when we use a pixel scale of 50 arcmin, as a visual example of this.

Smoothing

An alternative way to calculate the maps in a given smoothing scale is possible by using small pixels and applying a smoothing kernel of the corresponding scale to these pixels, instead of directly using large pixels. This smoothing scheme has two advantages. First of all, the area that can be used is optimized, since the pixels affected by the edges are only the closest to the mask (see Fig. 2 of Paper II). This is important for small areas and irregular masks. The other advantage of this scheme is that the maps produced give also a good visual image of the structures and how the field changes in the sky. However, the JK estimator has to be rescaled to obtain the correct errors, since neighbour JK subsamples are correlated due to the smoothing kernel. We address this in Paper II.

The results for a given scale are equivalent using this smoothing scheme or just enlarging the pixels, so in this paper we do not use any smoothing kernel in order to avoid the need of calibrating the JK estimator. For irregular masks, as in Paper II, smoothing allows to optimize the area used, and because of this we apply a smoothing kernel into very small pixels.

Exceptionally, in Figure 2 we apply the second scheme, and we use pixels of 7 arcmin and we apply a Top Hat filter of 50 arcmin to smooth the field. We do this only in this figure in order to have a better visibility of the structures of the maps and the shape of the area used. For the rest of the analysis of the paper, we use pixels of 50 arcmin and no

smoothing kernel afterwards. We then obtain the values of bias, and we do not need to rescale the JK errors obtianed.

Edge effects

We use a limited area and we project the sky to obtain the maps. When we pixelize the map with a definite pixel scale, due to the projection and the shape of the area used, part of the pixels in the edges are partially affected by the edges. We exclude these pixels from the analysis.

When a smoothing kernel is applied to the pixelized map, the pixels that are close to the edges are also affected by them. We exclude the pixels whose distance to the edges is smaller than the smoothing radius.

Source redshift

We estimate the κ field at $z \simeq 1.3$ by calculating the mean κ of the source galaxies with $1.2 < z < 1.4$ in each pixel. The redshift range used ensures we have enough density of galaxies to correctly calculate κ.

Theoretically one should take into account the redshift distribution of the source galaxies so that each galaxy contributes to κ_g with its position χ_s. However, approximating these galaxies to a plane in their mean position at $z \simeq 1.3$ causes less than a 1% effect.

Foreground galaxy redshift range

Equation (17) is strongly dependent on the redshift range used for the foreground galaxies. If we use only a partial redshift range for the construction of κ_g, the values of κ_g obtained have a lower amplitude, since in the sum we are missing the contribution coming from the unused redshift range. Moreover, as bias depends on redshift, using a wide redshift range for the foreground galaxies involves averaging this redshift dependent bias in the final result. However, this can be corrected for and used to obtain the bias in tomographic bins, as discussed in §3.5.

We use single redshift bins of $\Delta z = 0.2$ for the foreground galaxies in the range of $0.2 < z < 1.2$ to estimate the bias in each of these bins. This produces a galaxy bias estimation of 5 points in the whole redshift range available (for this method) in the simulation.

3.5 Redshift dependence

This method involves an integral (or a sum in practice) along the redshift direction, and because of this the bias obtained is a weighted average of the redshift dependent bias. However, we can estimate galaxy bias in a given redshift bin if we restrict the calculation to the foreground galaxies in that redshift bin, assuming that bias does not change significantly in the bin. If this is the case, we can measure the redshift-dependent bias using tomographic redshift bins.

Since κ_g is obtained from the contribution of all the galaxies in front of the sources, if we restrict the redshift range for the calculation of κ_g we need to renormalize the result by taking into account the contribution from the unused redshift range. Here is a description of the correction that we apply to estimate redshift dependent bias using tomographic bins.

Taking into account the sum from equation (17), and using δ instead of δ_g, we have:

$$\kappa(\boldsymbol{\theta}) = \sum_{all\ lens\ bins} \bar{q}' \delta'(\boldsymbol{\theta}) \Delta\chi', \qquad (23)$$

where we remind the reader that $\bar{q}'$ is the weak-lensing efficiency kernel of each bin. If we only use the foreground galaxies (or the dark matter field) in a single redshift bin between comoving coordinates χ_{min} and χ_{max}, then we call this partial convergence field κ', where

$$\kappa'(\boldsymbol{\theta}) = \bar{q}' \Delta\chi' \bar{\delta}' = \bar{q}' \Delta\chi' \int d\chi p'(\chi)\delta(\boldsymbol{\theta}, \chi), \qquad (24)$$

and

$$\bar{q}' = \int_{\chi_{min}}^{\chi_{max}} d\chi \frac{q(\chi)}{\Delta\chi}. \qquad (25)$$

$\Delta\chi = \chi_{max} - \chi_{min}$, and $p'(\chi)$ is the radial selection function (constant for the dark matter field in comoving coordinates, since the dark matter density is constant in these coordinates), normalized to 1 and restricted to the bin $\chi_{min} < \chi < \chi_{max}$. To simplify the notation, when the limits are not specified in the integral, the integral will go through the whole range between 0 and ∞. Note that, as $p'(\chi) = 0$ for all χ outside the bin, only the range $\chi_{min} < \chi < \chi_{max}$ contributes to the integral in equation (24), and $p'(\chi)$ implies a projection inside the bin. The factor $\bar{q}'$ appears to be outside the integral $\int d\chi p'(\chi)\delta(\boldsymbol{\theta}, \chi)$ when working in bins. This is exact for infinitely thin bins, and is also correct if $q(\chi)$ is not correlated with $p'(\chi)\delta(\chi)$ inside the bin. So, to summarize, the expression from equation (24) is affected by the projection in the bin, and the correlation between $q(\chi)$ and $p'(\chi)\delta(\chi)$.

For our purpose we are interested in the factors $\langle\kappa'\kappa\rangle$, $\langle\kappa'\kappa'\rangle$ and $\langle\kappa\kappa\rangle$ to be able to measure galaxy bias in tomographic redshift bins. According to these definitions, together with equation (15), we have:

$$\kappa'\kappa(\Theta) = \bar{q}' \Delta\chi' \int p'(\chi_1)d\chi_1 \int_0^{\chi_s} d\chi_2 q(\chi_2)\xi(r_{12}) \qquad (26)$$

$$\kappa'\kappa'(\Theta) = (\bar{q}' \Delta\chi')^2 \int p'(\chi_1)d\chi_1 \int d\chi_2 p'(\chi_2)\xi(r_{12}) \qquad (27)$$

$$\kappa\kappa(\Theta) = \int_0^{\chi_s} q(\chi_1)d\chi_1 \int_0^{\chi_s} q(\chi_2)d\chi_2\xi(r_{12}), \qquad (28)$$

with $r_{12}^2 = \chi_1^2 + \chi_2^2 + 2\chi_1\chi_2 \cos\theta$, $\xi(r_{12})$ is the 2PCF and Θ is the angular separation.

The quantities we are interested in are the ratios:

$$f_1 = \frac{\langle\kappa'\kappa\rangle}{\langle\kappa\kappa\rangle} \qquad (29)$$

and

$$f_2 = \frac{\langle\kappa'\kappa'\rangle}{\langle\kappa'\kappa\rangle} \qquad (30)$$

For the general case,

$$\langle\kappa_A\kappa_B\rangle = \frac{4\pi}{\pi^2 R^4}\int_0^R dr_1 r_1 \int_0^R dr_2 r_2 \int_0^\pi d\eta\,\omega_{AB}(\Theta), \quad (31)$$

where $\Theta^2 = r_1^2 + r_2^2 - 2r_1 r_2\cos\eta$, κ_A and κ_B can be κ, κ', κ_g or κ'_g, η is the angular separation between the vectors $\boldsymbol{r_1}$ and $\boldsymbol{r_2}$ and $\omega(\Theta)$ is the two-point angular correlation function of the two fields A and B, defined as

$$\omega_{AB}(\Theta) = \int_0^\infty d\chi_A \int_0^\infty d\chi_B\, q(\chi_A)q(\chi_B)p'(\chi_A)p'(\chi_B)\xi_{AB}(r),$$
$$(32)$$

where $p'(\chi_{A,B})$ are the corresponding selection functions of the fields A and B, and $\xi_{AB}(r)$ is the 3D two-point cross-correlation function, that in this case corresponds to the dark matter $\xi(r)$.

Equations (29,30) can be obtained analytically and they are weakly dependent on cosmology (the only dependence comes from the ratios between the lensing kernels). Equations (29,30) describe the contribution of these zero-lag correlations of κ in a given redshift bin for the dark matter field. As the dark matter field has a bias of 1 by definition, using the galaxies instead of the dark matter field to compute these equations would give $b'f_{1,2}$ instead of $f_{1,2}$, where b' is the galaxy bias in the redshift bin used (assuming that galaxy bias is constant inside the redshift bin). Then, to estimate galaxy bias in these bins, we need to obtain the bias from equations (18,19) using only the galaxies of these bins, and then rescale the bias according to the values of f_1 (or f_2) as described here:

$$b' = \frac{1}{f_1}\frac{\langle\kappa'_g\kappa\rangle}{\langle\kappa\kappa\rangle - \langle\kappa^N\kappa^N\rangle} \quad (33)$$

$$b' = \frac{1}{f_2}\frac{\langle\kappa'_g\kappa'_g\rangle - \langle\kappa'^N_g\kappa'^N_g\rangle}{\langle\kappa'_g\kappa\rangle}, \quad (34)$$

where κ'_g and κ'^N_g are obtained from the galaxies in a given redshift bin.

4   RESULTS

4.1   Testing

In this study we test our method against a fiducial galaxy bias. For this, we measure $\omega(\Theta)$ and $\omega_g(\Theta)$ of dark matter and galaxies in the simulation for different redshift bins, using the same area and galaxies that we use for our method. We also estimate bias from the definitions in equations (6-8) in the same simulation to study the consistency between the different bias definitions.

In Figure 3 we compare different estimations of galaxy bias from the MICE Simulation, using an area of $0^o < RA, DEC < 30^o$. The solid cyan line represents the bias definition from equation (3). We measure $\omega(\Theta)$ and $\omega_g(\Theta)$ as a function of the angular scale, and to obtain the bias we fit the ratio as constant between 6 and 60 arcmin. The angular correlation function involves different comoving scales for different redshifts, and then fixing the same
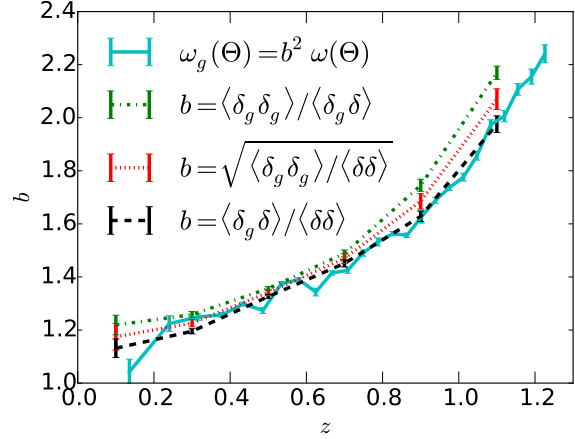

Figure 3. Comparison of different definitions of bias. Solid cyan line shows the bias as defined in equation (3). The dashed black, dash-dotted green and dotted red lines show bias according to the different definitions from equations (6-8).

angular scales for the galaxy bias implies a mix of physical scales. However, for large enough scales, bias is constant and is not affected by this. We have checked that bias is constant at these scales and in all redshift bins, an indication that we are in the linear regime. The galaxy bias obtained from equations (6-8) are shown in dashed black line, dotted red line and dash-dotted green line as specified in the legend. This has been calculated in each redshift bin by pixelating δ and δ_g in pixels of area $(50\text{ arcmin})^2$ using redshift bins of $\Delta z = 0.2$. The agreement between the solid cyan and the dashed black lines confirms that linear bias from $\omega(\Theta)$ converges to local bias at large scales. On the other hand, the differences in the different expressions of equations (6-8) implies a noise between δ_g and δ that affects our estimations of bias. The differences between these estimators can also be seen as an indirect measurement of this noise, that can come from stochasticity or other effects as projections and pixelization. We see that the same effect appears when using equation (37) to estimate galaxy bias, and this can be explained by the projection effect due to the redshift binning, as discussed below in Figures 4 and 5. We take into account this effect to estimate tomographic bias in §4.2.

For testing purposes, we construct here the bias-corrected κ_g map, $\hat{\kappa}_g$, defined as:

$$\hat{\kappa}_g(\boldsymbol{\theta}) = \sum_{all\ lens\ bins} q'\frac{\delta'_g(\boldsymbol{\theta})}{b'}\Delta\chi', \quad (35)$$

where b', or $b(z)$, corresponds to the linear bias that can be obtained from equations (3) or (6-8). In analogy with equations (18,19), we can calculate the corresponding normalized bias between the $\hat{\kappa}_g$ and κ fields:

$$\hat{b} = \frac{\langle\hat{\kappa}_g\kappa\rangle}{\langle\kappa\kappa\rangle - \langle\kappa^N\kappa^N\rangle} \quad (36)$$

$$\hat{b} = \frac{\langle\hat{\kappa}_g\hat{\kappa}_g\rangle - \langle\kappa^N_g\kappa^N_g\rangle}{\langle\hat{\kappa}_g\kappa\rangle}. \quad (37)$$
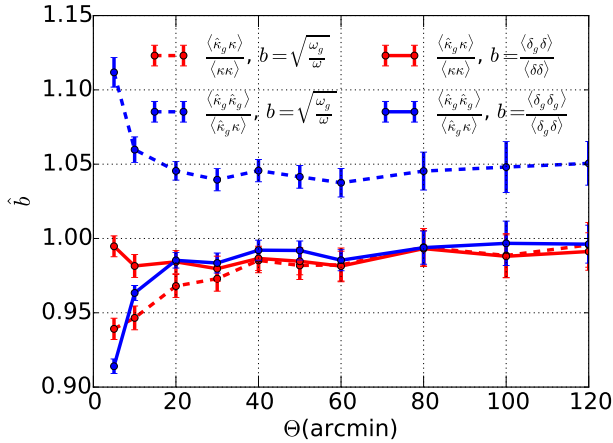
Figure 4. Normalized bias from the zero-lag cross correlations of κ and κ_g as a function of the angular smoothing scale, normalized by the redshift dependent bias from different estimators. Dashed red line shows $\langle \hat{\kappa}_g \kappa \rangle / \langle \kappa\kappa \rangle$, where $\hat{\kappa}_g$ has been obtained normalizing κ_g by the bias from equation (3). The solid red line shows the same, but normalizing κ_g from the bias obtained from $\langle \delta_g \delta \rangle / \langle \delta\delta \rangle$. For the dashed blue line, $\langle \hat{\kappa}_g \hat{\kappa}_g \rangle / \langle \hat{\kappa}_g \kappa \rangle$ has been obtained by normalizing $\hat{\kappa}_g$ by bias from equation (3). The solid blue line shows the same, but normalizing $\hat{\kappa}_g$ by the bias from $\langle \delta_g \delta_g \rangle / \langle \delta_g \delta \rangle$

Under this definition, $\hat{b} = 1$ suggests that this method is measuring linear bias, since it is basically assuming equation (5).

Figure 4 shows how the estimator $\hat{b}$ changes as a function of the angular scale, defined by the pixel scale, using different estimators of $\hat{b}$ and $b(z)$. For the dashed red and blue lines we used $b(z)$ from equation (3) to obtain $\hat{b}$ from $\langle \hat{\kappa}_g \kappa \rangle / \langle \kappa\kappa \rangle$ and $\langle \hat{\kappa}_g \hat{\kappa}_g \rangle / \langle \hat{\kappa}_g \kappa \rangle$ respectively (we omit the $\langle \kappa^N \kappa^N \rangle$ factors for visual simplicity). We can see that the measurements are constant for $\Theta > 30$ arcmin, meaning that we are in the linear regime in these scales. However, there is a 5% difference between the two estimators at large scales (at small scales nonlinearities appear and the difference is larger). This can be interpreted from Figure (3), where we see that the estimators $\langle \delta_g \delta \rangle / \langle \delta\delta \rangle$ and $\langle \delta_g \delta_g \rangle / \langle \delta_g \delta \rangle$ are slightly different. In fact, $\langle \hat{\kappa}_g \kappa \rangle / \langle \kappa\kappa \rangle$ is indirectly measuring $\langle \delta_g \delta \rangle / \langle \delta\delta \rangle$, which is consistent with bias from equation (3) (at the 1% level), while $\langle \hat{\kappa}_g \hat{\kappa}_g \rangle / \langle \hat{\kappa}_g \kappa \rangle$ is indirectly measuring $\langle \delta_g \delta_g \rangle / \langle \delta_g \delta \rangle$, which is slightly higher than bias from equation (3). If we use $b = \langle \delta_g \delta \rangle / \langle \delta\delta \rangle$ for the bias normalization of $\langle \hat{\kappa}_g \kappa \rangle / \langle \kappa\kappa \rangle$ (shown in the solid red line) and $b = \langle \delta_g \delta_g \rangle / \langle \delta_g \delta \rangle$ for the bias normalization of $\langle \hat{\kappa}_g \hat{\kappa}_g \rangle / \langle \hat{\kappa}_g \kappa \rangle$ (shown in the solid blue line), then both estimations are consistent, as expected. As in Figure 3 for b, the difference between both estimators of $\hat{b}$ coming from this test can be seen as an indication (and a measurement) of the noise in the relation between δ_g and δ, giving a factor of 5%.

In order to go deeper in the analysis of these numerical effects and see whether these differences between both estimators come from the intrinsic relation between δ_g and δ or from numerical systematics, we constructed the following
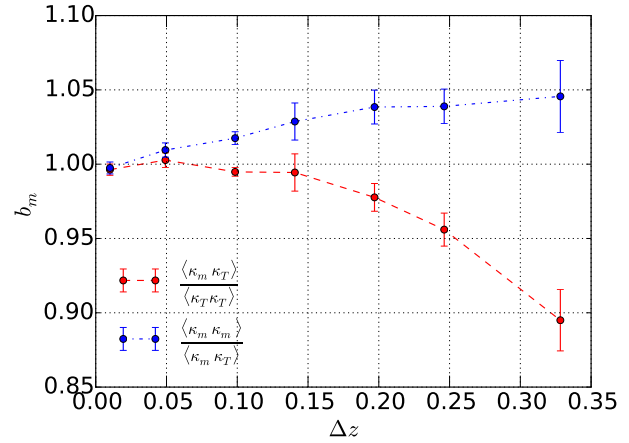

Figure 5. b_m, defined in equations (39,40), as a function of the redshift bin width used, Δz, for the two b_m estimators.

template κ_m:

$$\kappa_m(\boldsymbol{\theta}) = \sum_{i=0}^{N} q' \delta'(\boldsymbol{\theta}) \Delta\chi', \qquad (38)$$

which corresponds to the same exact calculation than equation (17) for κ_g, but using dark matter particles instead of galaxies. This field κ_m is expected to reproduce κ exactly except for the numerical differences between the method and how the original κ is obtained, which basically come from the redshift binning and projection discussed below equations (17,25). In order to avoid noise in the κ map, we use κ_T, defined as the true map directly obtained from the high resolution map of the simulation (see Gaztañaga & Bernardeau 1998; Fosalba et al. 2008, 2015b), and calculated the bias of these two estimators of κ as:

$$b_m = \frac{\langle \kappa_m \kappa_T \rangle}{\langle \kappa_T \kappa_T \rangle} \qquad (39)$$

$$b_m = \frac{\langle \kappa_m \kappa_m \rangle - \langle \kappa_m^N \kappa_m^N \rangle}{\langle \kappa_m \kappa_T \rangle}, \qquad (40)$$

that should give $b_m = 1$ if there are no numerical systematics.

We have found that b_m behaves as $\hat{b}$ in our tests, meaning that the differences between the different estimators can be seen as a measurement of the numerical effects on the method. In fact, we have found that the differences mainly come from the projection effect in the redshift bins, as shown in Figure 5. Here we show the two estimators of b_m as a function of the redshift bin width, Δz. We use a pixel scale of 50 arcmin, a source redshift of $z_s = 1$ and we use all the dark matter particles (diluted with respect to the total number of particles, but this does not affect the result) within $z < 1$. We see that the two estimators agree when we use narrow redshift bins, but the difference between both increases with Δz. For $\Delta z = 0.2$, the difference is the 5% that we see in Figure 4 for the galaxies. This test measures the redshift binning and the projection impacts on this method, and
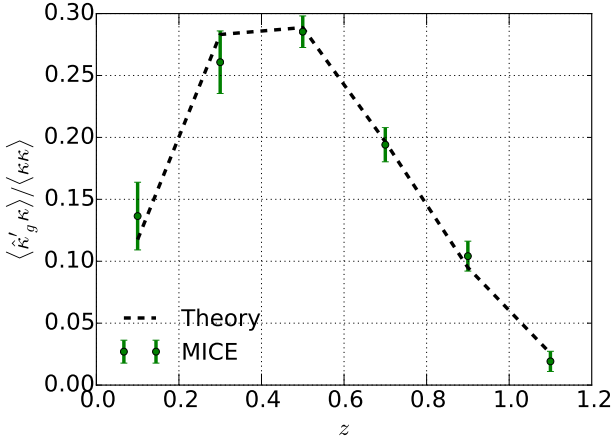
Figure 6. Comparison of $\langle \kappa' \kappa \rangle / \langle \kappa \kappa \rangle$ between theory (dashed black line) and simulation (green points). Each value has been obtained by using redshift bins of $\Delta z = 0.2$ to calculate κ', and using a source redshift of $z_s = 1.3$.

can also be used to calibrate the measurements. In fact, f_1 and f_2 can be used to take into account these projections, specified by the selection function $p'(\chi)$, and the redshift binning. But in the case of Figures 4 and 5, we use all the redshift range in the foreground of the sources and we have not corrected by f_1 and f_2. In the case of Figure 4, instead of using f_1 and f_2, we correct for this effect by using the bias which is estimated using the same redshift bin width as in the κ estimates. For narrow redshift bins these corrections are negligible. In the next section we will apply the f_1 and f_2 corrections to the tomographic estimations.

4.2 Redshift dependent bias

In Figure 6 we show a comparison between the theoretical predictions (in dashed black lines) of f_1 and the measurements in the MICE simulation (in green points) of $\langle \hat{\kappa}'_g \kappa \rangle / \langle \kappa \kappa \rangle$, in 6 different redshift bins of $\Delta z = 0.2$, using a redshift for the sources of $z_s = 1.3$. Here $\hat{\kappa}'_g$ is obtained from equation (35) but restricting the galaxies to each bin. To obtain the values for the simulation, we computed $\hat{\kappa}'_g$ in the corresponding bins, using $b = \langle \delta_g \delta \rangle / \langle \delta \delta \rangle$ for the normalization of κ_g. Then, $\hat{\kappa}'_g$ can be seen as an estimator of κ obtained from δ_g / b. We see a good agreement between theory and simulations. Note that the amplitude of f_1 is higher at the intermediate redshifts, due to the contribution of the lensing kernel, but this curve also reflects effects such as the projections due to the binning (so the fact that we ignore that $q(\chi)$ and $p'(\chi)\delta(\chi)$ might be correlated inside the bin), the correlation functions of different distances (so the fact that $\langle \kappa' \kappa \rangle$ has a contribution coming from the correlation between the dark matter distribution inside and outside the bin) or the redshift dependence of the smoothing scale of $\omega(\Theta)$ (different redshifts have different smoothing comoving scales). The final amplitude corresponds to f_1, so this reflects the contribution to $\hat{b}$ of each of these redshift bins.
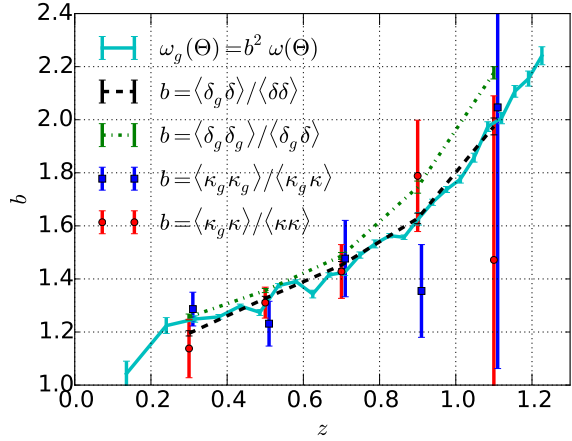

Figure 7. Redshift dependent bias estimated form our method, shown in red and blue points as specified in the legend. For this we used tomographic redshift bins of $\Delta z = 0.2$ and a source redshift of $z_s = 1.3$. The solid cyan line shows linear bias from equation (3), fitting bias as constant between 6 and 60 arcmin. The dashed black line shows bias estimated from $\langle \delta_g \delta \rangle / \langle \delta \delta \rangle$, using the same redshift bins of $\Delta z = 0.2$. The dash-dotted green line shows bias estimaed from $\langle \delta_g \delta_g \rangle / \langle \delta_g \delta \rangle$ in the same redshift bins.

Equations (33,34) give a tool that can be used for tomographic measurements of galaxy bias, since we can estimate the bias using different redshift bins of the foreground galaxies if we take this correction into account. That is, we can measure b' for a given redshift by calculating κ'_g in that bin and using equations (33,34).

Figure 7 shows the estimation of the tomographic bias using different redshift bins of $\Delta z = 0.2$ for both estimators from equations (33,34), represented as blue and red points as specified in the legend. We compare them with the fiducial bias from equations (3,6,7) shown in solid cyan, dashed black and dash-dotted green lines respectively. We see that the method we present in this paper gives consistent results with linear bias. There are some slight differences for the estimator from equation (7) which, as mentioned above, is due to the effects of projection and binning. But this effect is not shown from the tomographic bias obtained from our method, because we take into account these effect in the factors f_1 and f_2. Note also that the two methods, represented by the red and blue points, give very similar results (apart from the fourth bin).

We can see that the errors are very large for the highest redshift bin. This is due to the fact that, due to the lensing kernel, f_1 and f_2 are very small, and then the measurements in this bin are very sensitive to small changes. The best error bars appear where the lensing kernel is higher, so the potential of this method is optimal in the maximum of the lensing kernel. Hence, different source redshifts might be combined in order to optimize the analysis for all redshifts. In Paper II we combine the results using multiple redshift bins for the source galaxies, and we fit the galaxy bias from the combination of these measurements, using both κ_g and γ_g and doing a full-covariance analysis. In this paper we do not ap-

ply any fit, since we directly measure bias from equations (33,34) using a fixed source redshift bin.

This study proves that we can use this method to measure linear bias, since our method is consistent with the linear bias measured from equation (3). This method has some advantages with respect to other estimators of bias. First of all, it can be applied to observations, as discussed in §4.3. In this case, we do not need to assume a dark matter distribution, since we can obtain this information from the weak lensing maps, and hence this method is able to measure bias from the direct comparison between the galaxy and dark matter distributions. Moreover, this method does not depend strongly on σ_8, as most of the common methods to measure bias. However, it depends on Ω_m, but it is weakly dependent on the other cosmological parameters. The combination of this method with other estimators of bias that depend on σ_8 allow us to constrain at the same time bias and cosmology. Because of this, this method is a very good complement to other measurements of bias.

4.3 Application to data

When applying this method to data, we need to take into account other aspects for the measurements. First of all, we cannot measure κ directly from observations, since the lensing information comes from the ellipticity of the galaxies. Then, we need to obtain γ from the measured ellipticities, assuming some shape noise, and then convert γ to κ or κ_g to γ_g to measure bias from equations (18,19) or (21,22). Vikram et al. (2015) explored the conversion from ellipticities to κ for the DES SV data, obtaining the largest mass map from weak lensing ever observed. They also showed the consistency between the mass map and the foreground galaxy distribution. However, it is important to mention that, since shape noise is the most important source of uncertainty for this method in observations, the terms $\langle \kappa\kappa \rangle$ and $\langle \gamma\gamma \rangle$ are very noisy and need to be avoided for an optimal analysis.

Moreover, for photometric surveys we need to take into account the photo-z estimation. The uncertainty in the redshift of the galaxies causes an smoothing of κ_g that has to be calibrated from the understanding of the photo-z errors, as well as from the distribution of the galaxies in redshift. This has to be taken into account when defining the selection functions in the calculation of f_1 and f_2.

Other aspects from observations, such as the mask and the shape measurements, can affect our measurements and must be taken into account. We address these aspects in Paper II where we measure bias in DES SV using the method presented here.

5 DISCUSSION AND CONCLUSIONS

In this paper we explore a new method to measure galaxy bias from the combination of the galaxy density and weak lensing fields. This method is based on Amara et al. (2012), where they use the galaxy density field to construct a bias-weighted convergence map κ_g in the COSMOS field. They measure different parameterizations of galaxy bias from the

zero-lag correlations of the galaxy shear and a reconstruction of the shear from the galaxy density field. In this paper we present a new way to measure tomographic bias from the zero-lag correlations between the lensing maps and a reconstruction of the lensing maps from the galaxy density field. We also study the robustness and the systematics of this method for the first time.

The implementation of this model is as follows. We construct a template of the convergence field κ_g at the source redshift by integrating the density field of the foreground galaxies in the line-of-sight weighted by the corresponding lensing kernel as specified in equation (16). We do this for tomographic bins in the lens distribution. We then compare to estimates of the matter convergence map κ associated to the same galaxies in the source redshift bin. We measure galaxy bias from the smoothed zero-lag cross-correlations between κ and κ_g as in equations (18,19). Instead of using the zero-lag cross-correlation we could also use the 2-point cross-correlation function.

We use the MICE simulations to study the consistency of our method by comparing our results with a fiducial galaxy bias measurement on linear scales. This is obtained from the ratio between the projected 2PCFs ($\omega(\Theta)$) of galaxies and dark matter as a function of redshift (see equation (3)), and fitting a constant galaxy bias between 6 arcmin and 60 arcmin. We also study local bias from equations (6-8), making use of the dark matter field of the simulation. With these comparisons we study the systematics of the method and the regimes where it is consistent with linear bias.

There are different systematic effects and numerical dependencies of the method that need to be taken into account for a correct measurement of linear bias. First of all, the method is sensitive to the redshift bin width used in the construction of κ_g, that have an impact on the galaxy bias estimators due to the projection effects of the density fields. This causes differences in the values obtained for the different estimators, that can be larger than 5% for $\Delta z > 0.2$ and larger than 10% for $\Delta z > 0.3$. This has to be taken into account when measuring κ_g in wide redshift bins in order to obtain the correct linear bias. On the other hand, projecting the source galaxies in a plane have an insignificant impact on the results. Secondly, the angular smoothing scale of the field can be affected by nonlinearities for small enough scales. We find that the measurements are consistent with linear bias for angular scales of $\Theta > 30$ arcmin, where bias is constant. Sampling and discreteness noise is also important and needs to be taken into account (see equations (18,19)). Finally, we need to exclude from the analysis those pixels that are affected by the edges of the area used.

A correction must be applied to our estimators if we only use the foreground galaxies in a given redshift bin for the construction of κ_g. This is because the amplitude of κ_g is reduced by the fact that we do not use all the information from the complete redshift range in front of the source redshift. We predict theoretically this effect, and we find good agreement with the measurements, indicating that we can use this prediction to correct the bias obtained. The theoretical prediction describes the amplitude of the zero-lag corre-

lations obtained using a given redshift bin for the foreground dark matter field, that by definition has a bias of 1. We can measure galaxy bias in that bin from the ratio between the zero-lag correlations of κ and κ_g (using the foregroud galaxies in that bin) and the theoretical prediction. This provides a useful tool to do tomography and measure galaxy bias in single redshift bins. We measure and show the redshift-dependent bias obtained using this method, and find good agreement with the redshift-dependent bias from equation (3).

Other issues associated with observational data must be addressed if we apply this method to large galaxy surveys such as the Dark Energy Survey (DES). First of all, we measure γ instead of κ from the ellipticities of the galaxies, but we obtain κ_g from the galaxy density field. Thus, we need to apply a conversion from κ_g to γ_g or from γ to κ in order to calculate the zero-lag correlations. This conversion is affected by the shape of the mask and the noise of the maps. Secondly, for photometric surveys we need to account for the photo-z estimation. The uncertainty on the redshift of the galaxies causes a smoothing in κ_g that needs to be corrected from the photo-z errors and the galaxy redshift distribution. Other effects in observations include the boundary effects of irregular masks, that affect the useful area of the analysis, and shape noise, that causes some of the estimators to be very noisy. We apply this method to the DES Science Verification data in a follow-up paper (Chang et al. in prep). This method is expected to be significantly better when applied to larger areas, such as in DES Year 1 (Diehl et al. 2014) or the 5000 deg^2 from the expected total area of the DES survey.

This paper presents the method, but further studies can be done. We can explore galaxy bias for different galaxy samples, e.g. as a function of colour and luminosity. We can also explore the scale dependence of local bias by studying different angular scales and its nonlinearities, and the redshift dependence by comparing the tomographic measurements with parametric redshift-dependent bias based on Amara et al. (2012). In this paper we have focused on zero-lag cross-correlations, but we could also use 2-point cross-correlations as a way to estimate the bias and include the redshift cross-correlations as a validation test.

The method studied in this paper has several attractive features. First of all, there is no need to assume a dark matter distribution to measure bias, since this distribution is measured from the weak lensing field. This method is then a direct way to measure local bias by comparing the observed galaxy and dark matter distributions. Moreover, the method depends very weakly on σ_8 (only in non-linear corrections to f_1 and f_2), while other measurements of bias are typically strongly dependent on σ_8. On the other hand, it depends on Ω_m. Hence, a combined analysis of different measurements of galaxy bias, including this method, can be very useful to constrain better bias and cosmology. Second, the method can be applied to a situation where galaxies only cover partially the full redshift range of the lenses. Moreover, the potential of this method will rapidly increase with the data of present and upcoming surveys, such as the Hyper Suprime-Cam (HSC), the Dark Energy Survey (DES),

the Kilo Degree Survey (KiDS), the Large Synoptics Survey Telescope (LSST), the Wide-Field Infrared Survey Telescope (WFIRST) and the Euclid mission.

REFERENCES

Amara A. et al., 2012, MNRAS, 424, 553
Angulo R. E., Baugh C. M., Lacey C. G., 2008, MNRAS, 387, 921
Bartelmann M., Schneider P., 2001, PhysRep, 340, 291
Bel J., Hoffmann K., Gaztañaga E., 2015, ArXiv e-prints
Bernardeau F., 1996, A&A, 312, 11
Bernardeau F., Colombi S., Gaztañaga E., Scoccimarro R., 2002, PhysRep, 367, 1
Blanton M. R. et al., 2003, ApJ, 592, 819
Blanton M. R., Lupton R. H., Schlegel D. J., Strauss M. A., Brinkmann J., Fukugita M., Loveday J., 2005a, ApJ, 631, 208
Blanton M. R. et al., 2005b, *Aj* , 129, 2562
Cacciato M., Lahav O., van den Bosch F. C., Hoekstra H., Dekel A., 2012, MNRAS, 426, 566
Carretero J., Castander F. J., Gaztañaga E., Crocce M., Fosalba P., 2015, MNRAS, 447, 646
Cole S., Kaiser N., 1989, MNRAS, 237, 1127
Coupon J. et al., 2012, A&A, 542, A5
Crocce M. et al., 2015a, ArXiv e-prints
Crocce M., Castander F. J., Gaztañaga E., Fosalba P., Carretero J., 2015b, MNRAS, 453, 1513
de Jong J. T. A. et al., 2013, The Messenger, 154, 44
Di Porto C. et al., 2014, ArXiv e-prints
Diehl H. T. et al., 2014, in Society of Photo-Optical Instrumentation Engineers (SPIE) Conference Series, Vol. 9149, Society of Photo-Optical Instrumentation Engineers (SPIE) Conference Series, p. 0
Durkalec A. et al., 2014, ArXiv e-prints
Eriksen M., Gaztanaga E., 2015, ArXiv e-prints
Faltenbacher A., White S. D. M., 2010, ApJ, 708, 469
Flaugher B., 2005, International Journal of Modern Physics A, 20, 3121
Fosalba P., Crocce M., Gaztañaga E., Castander F. J., 2015a, MNRAS, 448, 2987
Fosalba P., Gaztañaga E., Castander F. J., Crocce M., 2015b, MNRAS, 447, 1319

Fosalba P., Gaztañaga E., Castander F. J., Manera M., 2008, MNRAS, 391, 435

Fry J. N., Gaztanaga E., 1993, ApJ, 413, 447

Gaztanaga E., Bernardeau F., 1998, A&A, 331, 829

Green J. et al., 2012, ArXiv e-prints

Hoffmann K., Bel J., Gaztañaga E., Crocce M., Fosalba P., Castander F. J., 2015, MNRAS, 447, 1724

Jullo E. et al., 2012, ApJ, 750, 37

Kaiser N., 1984, *ApJL*, 284, L9

Kaiser N. et al., 2010, in Society of Photo-Optical Instrumentation Engineers (SPIE) Conference Series, Vol. 7733, Society of Photo-Optical Instrumentation Engineers (SPIE) Conference Series, p. 0

Kaiser N., Squires G., 1993, ApJ, 404, 441

Kravtsov A. V., Klypin A. A., 1999, ApJ, 520, 437

Laureijs R. et al., 2011, ArXiv e-prints

LSST Science Collaboration et al., 2009, ArXiv e-prints

Manera M., Gaztañaga E., 2011, MNRAS, 415, 383

Manera M., Sheth R. K., Scoccimarro R., 2010, MNRAS, 402, 589

Marín F. A. et al., 2013, MNRAS, 432, 2654

Massey R. et al., 2007, Nature, 445, 286

Miyazaki S. et al., 2006, in Society of Photo-Optical Instrumentation Engineers (SPIE) Conference Series, Vol. 6269, Society of Photo-Optical Instrumentation Engineers (SPIE) Conference Series, p. 0

Mo H. J., White S. D. M., 1996, MNRAS, 282, 347

Paranjape A., Sefusatti E., Chan K. C., Desjacques V., Monaco P., Sheth R. K., 2013, MNRAS, 436, 449

Pollack J. E., Smith R. E., Porciani C., 2014, MNRAS, 440, 555

Pujol A., Gaztañaga E., 2014, MNRAS, 442, 1930

Pujol A., Hoffmann K., Jiménez N., Gaztañaga E., 2015, ArXiv e-prints

Refregier A., 2003, *ARA&A*, 41, 645

Roth N., Porciani C., 2011, MNRAS, 415, 829

Seljak U., Warren M. S., 2004, MNRAS, 355, 129

Sheth R. K., Tormen G., 1999, MNRAS, 308, 119

The Dark Energy Survey Collaboration, 2005, ArXiv Astrophysics e-prints

Tinker J. L., Robertson B. E., Kravtsov A. V., Klypin A., Warren M. S., Yepes G., Gottlöber S., 2010, ApJ, 724, 878

Van Waerbeke L. et al., 2013, MNRAS, 433, 3373

Vikram V. et al., 2015, ArXiv e-prints

White S. D. M., Rees M. J., 1978, MNRAS, 183, 341

Zehavi I. et al., 2011, ApJ, 736, 59

Zentner A. R., Hearin A. P., van den Bosch F. C., 2014, MNRAS, 443, 3044